# CHAPTER 4

*Fenton reaction by $H_2O_2$ produced on magnetically recyclable $Ag/CuWO_4/NiFe_2O_4$ photocatalyst*

## 4.1 INTRODUCTION

This chapter explores a magnetically recyclable visible-light-driven composite photocatalyst, Ag/$NiFe_2O_4$/CuWO4, for $H_2O_2$ production. Its photocatalyst components were selected using two key factors. First, the VB and CB positions of the individual photocatalysts. Second, efficient $H_2O_2$ production via photocatalysis requires effective oxygen adsorption on the reduction component of the composite. Therefore, ensuring a strong affinity of $O_2$ for the reduction component is crucial. Classical molecular dynamics (MD) simulations can provide reasonably accurate predictions of this affinity [49,144].

$CuWO_4$, an n-type visible-light-responsive semiconductor photocatalyst, has a moderate band gap of approximately 2- 2.5 eV, high chemical stability, easy fabrication at low cost, and a positive VB position [145]. The latter makes it favorable for water oxidation [146–148]. $NiFe_2O_4$, a magnetic semiconductor, is the other component of the planned composite photocatalyst. It has complementary VB and CB positions and an energy gap in the 1.8-2.3 eV range [149,150]. Depending on the synthesis protocol, it could be a p-type or n-type semiconductor photocatalyst. Nanosized $NiFe_2O_4$ particles provide a larger surface area and superparamagnetic properties [151]. Heterojunctions with such a component can be easily recycled via magnetic decantation. Finally, the deposition of silver metal on the composite surface can enhance the photocatalytic reaction rate. Ag nanoparticles (NPs) act as electron capture centers and suppress electron-hole recombination [49]. In addition, Ag NPs show interesting 2e- $O_2$ reduction behavior and oxygen adsorption properties [41,152–154].

There is no previous report on the photocatalytic $H_2O_2$ formation properties of the magnetically recyclable Ag/$CuWO_4$/$NiFe_2O_4$ composite. Furthermore, the $H_2O_2$ produced is used for in situ Fenton-like degradation of tetracycline. The photocatalyst was prepared by a step-wise precipitation method. XRD, TEM, and XPS techniques investigated the

phases in the composite, morphologies of the particles, and oxidation states of the elements present. A large-scale classical MD simulation investigated the oxygen and water adsorption affinity towards respective semiconductor components. Extensive control experiments helped gain insight into the operating photocatalytic mechanism.

## 4.2 EXPERIMENTAL SECTION

### 4.2.1 Synthesis of $NiFe_2O_4$

Initially, Ni $(NO_3)_2{\cdot}6H_2O$ (3.15 mmol) and Fe $(NO_3)_2{\cdot}2H_2O$ (6.3 mmol) were dissolved in 70 mL of DW. The mixture was continuously stirred for 3 hours. Then, an appropriate volume of 2M NaOH solution was added to bring the pH value of the reaction mixture to 13. Next, the reaction mixture was heated at 80°C for one hour under vigorous stirring. The precipitate formed was centrifuged, rinsed ten times with distilled water (DW)/ethanol, and dried at 60°C for 24 hours. The dried powder was calcined at 400°C for 3 hours.

### 4.2.2 Synthesis of $CuWO_4$

In this experiment, 0.77 mmol of $Cu(NO_3)_2{\cdot}6H_2O$ and 0.77 mmol of $Na_2WO_4{\cdot}2H_2O$ were dissolved separately in 30 mL of DI water to create two distinct solutions.18 Then, 1 wt% poly (N-vinyl pyrrolidone) (PVP) was added to the Cu $(NO_3)_2{\cdot}6H_2O$ solution. Subsequently, the $Cu(NO_3)_2{\cdot}6H2O$ solution was gradually mixed with the $Na_2WO_4{\cdot}2H_2O$ solution while being continuously stirred for 2 hours. A sea-green precipitate was formed as a result of this process. The precipitate was dried at 70 °C for 20 hours and then repeatedly washed with DI water and ethanol before being calcined at 500 °C for 3 hours.

### 4.2.3 Synthesis of $NiFe_2O_4$/$CuWO_4$ nanocomposite

Precisely 360 mg of previously prepared $NiFe_2O_4$ nanoparticles were re-dispersed in 20 ml of DW by bath sonication for 10 min. Separate solutions of 0.77 mmol $Cu(NO_3)_2.6H_2O$ and 0.77 mmol $Na_2WO_4.2H_2O$ were prepared in 30 mL of DW each. The re-dispersed $NiFe_2O_4$ nanoparticles were added to the $Cu(NO_3).6H_2O$ solution and stirred for 2 hours. Then, 1 wt. % of polyvinyl pyrrolidone (PVP) was added to this mixture. The $Na_2WO_4.2H_2O$ solution prepared earlier was gradually added to the above reaction mixture and stirred for 2 hours. The composite was isolated from the solution with the magnet, washed three times with ethanol, dried at 60°C for 12 hours, and calcined at 500°C. The prepared composite sample was coded as U1 for $CuWO_4$/$NiFe_2O_4$ composite.

### 4.2.4 Synthesis of silver loaded $CuWO_4$/$NiFe_2O_4$ nanocomposite

Different weight percentages (wt%) of Ag (2.5, 5, and 10 wt% %) nanostructures were precipitated on $CuWO_4$/$NiFe_2O_4$ nanocomposites. In detail, 300mg $CuWO_4$/$NiFe_2O_4$ was dispersed in the 40 ml DW using a sonication bath. Next, a calculated amount of $AgNO_3$ (required for the desired weight percent) was added to the above-dispersed solution. After that, an appropriate amount of $NaBH_4$ was added to the prepared mixture. The pH of the reaction mixture was adjusted to 8 with 0.5M NaOH. Lastly, the whole suspension was heated at 60°C for one hour. The product was separated magnetically. It was washed ten times with DW/ethanol and then dried at 50°C for 24 hours. The composites prepared are abbreviated as 2.5AgU1, 5AgU1, and 10AgU1, depending on the weight percent of $AgNO_3$ used in the synthesis. Scheme 4.1 shows the synthesis pathway of Ag/$CuWO_4$/$NiFe_2O_4$ formation.

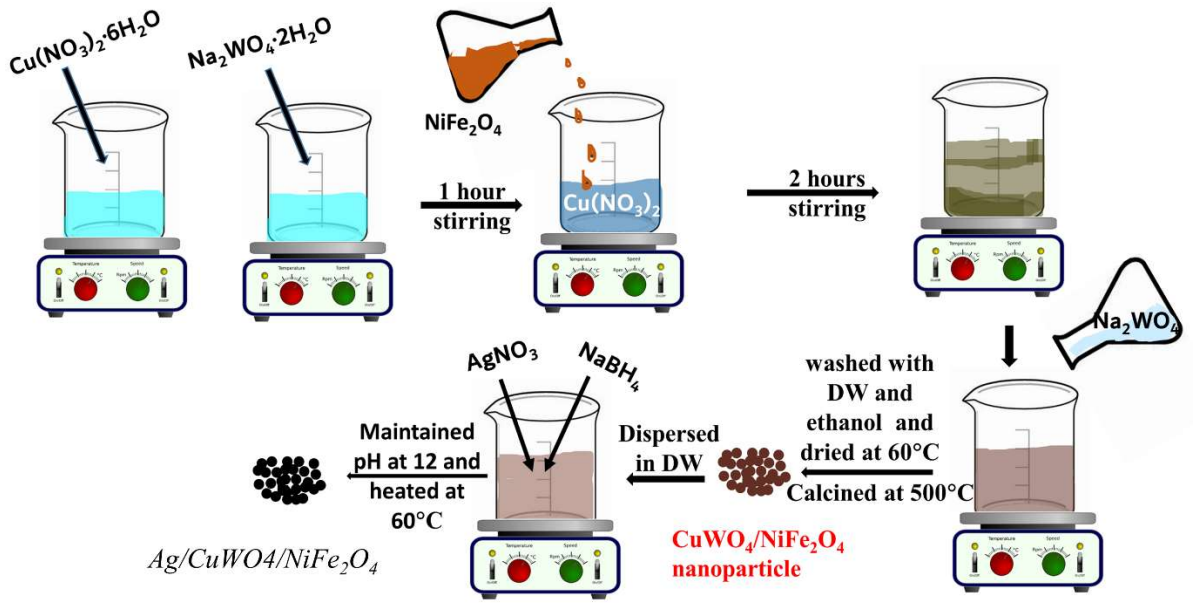


**Scheme 4.1** Schematic representation of the synthesis pathway of Ag/$CuWO_4$/$NiFe_2O_4$ formation.

### 4.2.5 Photocatalytic $H_2O_2$ production

In a typical process, 5mg of the composite sample was dispersed into 10 ml of DW using a sonication bath (20 min). Then 500µl of the re-dispersed photocatalyst was mixed with 6 ml of distilled water in a 15 ml borosilicate glass vial. The vial was completely sealed with a rubber septum, and $O_2$ gas was continuously passed through the suspension. The reaction vessel was then kept in the dark for an hour. Afterward, it was irradiated with visible light (cool white LED) for one hour. The formation of $H_2O_2$ was estimated by titrating the reaction mixture (after magnetically removing the photocatalyst nanoparticles) against an acidified (standardized) $KMnO_4$ solution. Additionally, an iodometric method using absorbance spectroscopy was also employed to quantitatively verify the $H_2O_2$ production over the photocatalyst exhibiting the best activity. The details of this $KMnO_4$ titration and iodometric methods for $H_2O_2$ estimation are given in Chapter 2.

The experiment also assessed the photocatalyst for $H_2O_2$ production under different pH conditions. Comparative experiments were carried out under other control conditions as well. These included experiments with water containing 5 vol% % ethanol and water containing 5 vol% isopropyl alcohol (IPA) mixture with continuous $O_2$ purging. The effect of adding p-benzoquinone (PBQ), a superoxide scavenger, was also studied.

### 4.2.6 Photocatalytic degradation of tetracycline

The prepared photocatalyst was evaluated for the degradation of tetracycline under $H_2O_2$ production reaction conditions. In this reaction, 5 mg of the photocatalyst was dispersed in 10 mL of DW. Then 250 $\mu l$ of the re-dispersed photocatalyst sol was added to 3 ml DW in the actual photocatalysis experiment. The reaction was performed in a 3.5 ml four-sided transparent cuvette. The above-prepared mixture was kept in the dark for 40 min to achieve adsorption-desorption equilibrium. Afterward, it was irradiated with visible light from a cool white LED source and continuous oxygen purging. The absorbance of the undegraded tetracycline was directly monitored at regular intervals over time using a UV-visible spectrophotometer. The photocatalyst was magnetically recovered after completing one degradation cycle. It was then washed five times with DW/ethanol, dried, and reused for the next cycle. Isopropanol (IPA, hydroxyl radical scavenger), potassium iodide (KI hole ($h^+$) quencher), and p-benzoquinone (PBQ, superoxide ion ($\cdot O_2^-$) quencher) were used to trap separate reactive species generated during the reaction. Another experiment was carried out on an aqueous tetracycline solution containing 5-vol% ethanol under $O_2$ purging.

### 4.2.7 Model building and MD simulation

The Scienomics MAPS 4.01 molecular modeling software was used to construct the supercells of $CuWO_4$ and $NiFe_2O_4$. A triclinic unit cell of $CuWO_4$ (mp-22773) and a cubic unit cell of $NiFe_2O_4$ (mp-22684) were used for this purpose. $CuWO_4$ and $NiFe_2O_4$

supercells were cleaved at (100) and (311) planes using the surface builder tool in MAPS 4.01 to construct slabs of dimensions 35.97 Å ×34.96 Å ×7 Å and 34.84 Å ×35.55 Å ×7 Å, respectively. The $CuWO_4$ slab was placed in the middle of a 34.84Å ×35.55Å ×57 Å rectangular (parallelepiped) simulation box. Again, the $NiFe_2O_4$ slab was positioned in the middle of a 35.97Å ×34.96Å ×57 Å parallelepiped simulation box. Water and oxygen molecules were built using the molecule builder plugin in MAPS and optimized using the Modified Neglect of Diatomic Overlap (MNDO) method. The TIP3P water model was used in these simulation studies. Ten oxygen and eight hundred water molecules were inserted on each side of the $CuWO_4$ slab in the model system. The empty space in the $NiFe_2O_4$ simulation box was also filled up similarly with $O_2$ and $H_2O$ molecules (Figure 4.1). The density of the liquid phase in these systems was ~ 1.01 g/cc. After an initial conjugate gradient optimization, these systems were subjected to MD simulations using the LAMMPS (Large-scale Atomic/Molecular Massively Parallel Simulator) program. Periodic boundary conditions were applied to all three dimensions of the simulation cell. The temperature was 298.15 K for both simulation systems. Each system was subjected to MD simulation in the NVT ensemble for ten ns simulation time using a time step of 1 fs. The particle mesh approach with a 12 Å cut-off distance was used to calculate Coulombic interactions. All atoms of the oxide slab remained fixed through the simulation in each model. The simulation was conducted for a total of 10 nanoseconds (ns), with the first 7 ns for equilibration and the remaining 3 ns as the production run.

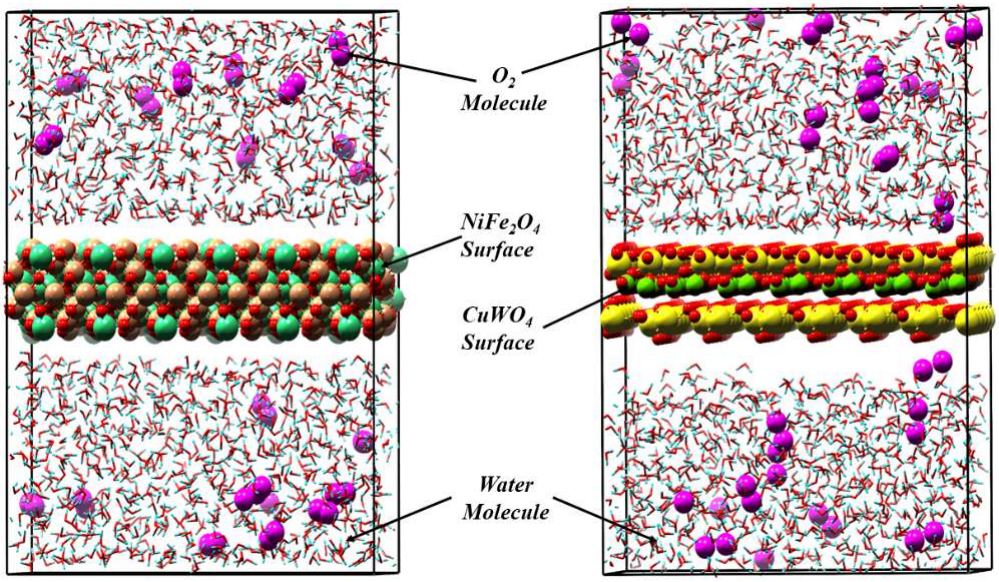


**Figure 4.1** A snapshot of the model after insertion of 20 $O_2$ and 1600 $H_2O$ molecules in the simulation cell (left side-$NiFe_2O_4$ (311) & right side $CuWO_4$ (100) simulation model).

## 4.3 RESULTS AND DISCUSSION

Figure 4.2 displays XRD patterns of the $CuWO_4$, $NiFe_2O_4$, U1, 2.5AgU1, 5AgU1, and 10AgU1 powder samples. The XRD pattern of $NiFe_2O_4$ could be indexed to the cubic spinel (JCPDS No #89-4927) structure. Its peaks at 18.42°, 30.23°, 35.67°, 37.29°, 43.37°, 53.82°, 57.38°, and 63.02° were assigned to the (111), (220), (311), (222), (400), (422), (511) and (440) planes of $NiFe_2O_4$. Fine crystallite sizes give rise to broadened XRD peaks for the $NiFe_2O_4$ sample. The $CuWO_4$ diffraction peaks at $2\theta$ values of 15.28°, 18.99°, 28.66°, 30.10°, 31.60°, 32.2°, and 55.61° are indexed to (0 1 0) (1 0 0) ($\bar{1}$11) (1 $\bar{1}$1) ($\bar{1}$ $\bar{1}$1) (1 1 1) and (202) triclinic crystal planes of JCPDS file 88–0269. No new phases were observed in the XRD of the composite sample U1. A few peaks in the XRD of the composite U1 got broadened because of the overlap of some broad $NiFe_2O_4$ and $CuWO_4$ peaks.

Similarly, the XRD patterns of 2.5AgU1, 5AgU1, and 10AgU1 samples show peaks of $NiFe_2O_4$ and $CuWO_4$ phases, demonstrating the successful formation of the

$CuWO_4$/$NiFe_2O_4$ nanocomposite. The XRD patterns of 2.5AgU1, 5AgU1, and 10AgU1 composites also display peaks at $2\theta$ values of 38.23°, 44.34°, and 64.44°. These peaks are ascribed to the (111), (200), and (220) crystal planes of the FCC Ag phase. Thus, these three samples have Ag nanostructures loaded on the $CuWO_4$/$NiFe_2O_4$ composite.

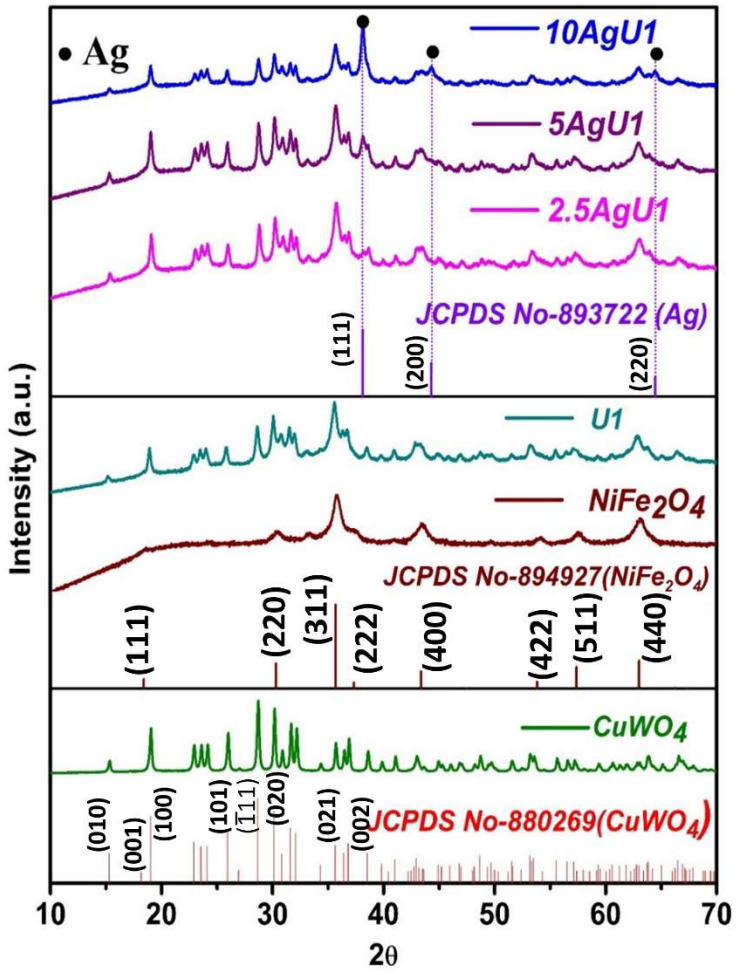


**Figure 4.2** Displays the XRD patterns of all samples prepared in this work.

Figure 4.3 shows the TEM images of $NiFe_2O_4$, $CuWO_4$, U1, and 5AgU1 nanoparticles. The TEM images in Figures 4.3a and 4.3c reveal that the $NiFe_2O_4$ and $CuWO_4$ particles are nearly spherical, with average particle sizes of 9.5 nm and 80 nm, respectively. The HR-TEM images of pristine $NiFe_2O_4$ and $CuWO_4$ are presented in Figures 4.3b and 4.3d, respectively. Figure 4.3b shows lattice fringes with a spacing of 0.25 nm, corresponding to

the (311) crystal plane of $NiFe_2O_4$. Similarly, Figure 4.3d displays lattice fringes with a spacing of 0.467 nm, attributed to the (100) crystal plane of $CuWO_4$.

Figure 4.3e displays the TEM image of the $NiFe_2O_4$/$CuWO_4$ (U1) nanocomposite. The corresponding HR-TEM image, highlighting a selected region from the composite TEM image, is shown in Figure 4.3f. This image reveals two types of lattice fringes with different interplanar spacings attributed to adjacent nanostructures within the composite. Figure 4.3g presents the inverse fast Fourier transform (IFFT) images of the U1 composite, confirming the presence of the (311) plane of $NiFe_2O_4$ and the (100) plane of $CuWO_4$. These observations are consistent with the HR-TEM images of pure $NiFe_2O_4$ and $CuWO_4$ nanoparticles shown in Figures 4.3b and 4.3d, respectively. The proximity of the adjacent fringes provides direct evidence for the formation of $CuWO_4$/$NiFe_2O_4$ heterostructures. It further confirms that the finer particles correspond to the $NiFe_2O_4$ phase, while the larger particles represent the $CuWO_4$ phase. Therefore, Figure 4.3e demonstrates that the $NiFe_2O_4$ nanostructures are deposited on the surface of the $CuWO_4$ nanoparticles, with $NiFe_2O_4$ appearing as the smaller structures and $CuWO_4$ as the larger ones.

Figure 4.3h depicts a TEM image of the 5AgU1 sample. The Ag nanoparticles (indicated by red encircled regions) are uniformly distributed over the composite nanoparticles. Neighboring FCC (111) Ag and $NiFe_2O_4$ (311) lattice fringes demonstrate the formation of Ag nanostructures on the ($NiFe_2O_4$/$CuWO_4$) composite (Figure 4.3h). The low-resolution SEM images and their corresponding elemental distribution profile of 5AgU1 material are presented in Figure 4.3 (i, j). The presence of Cu, W, Fe, Ni, O, and Ag in required stoichiometry is observed from the EDX study of FESEM.

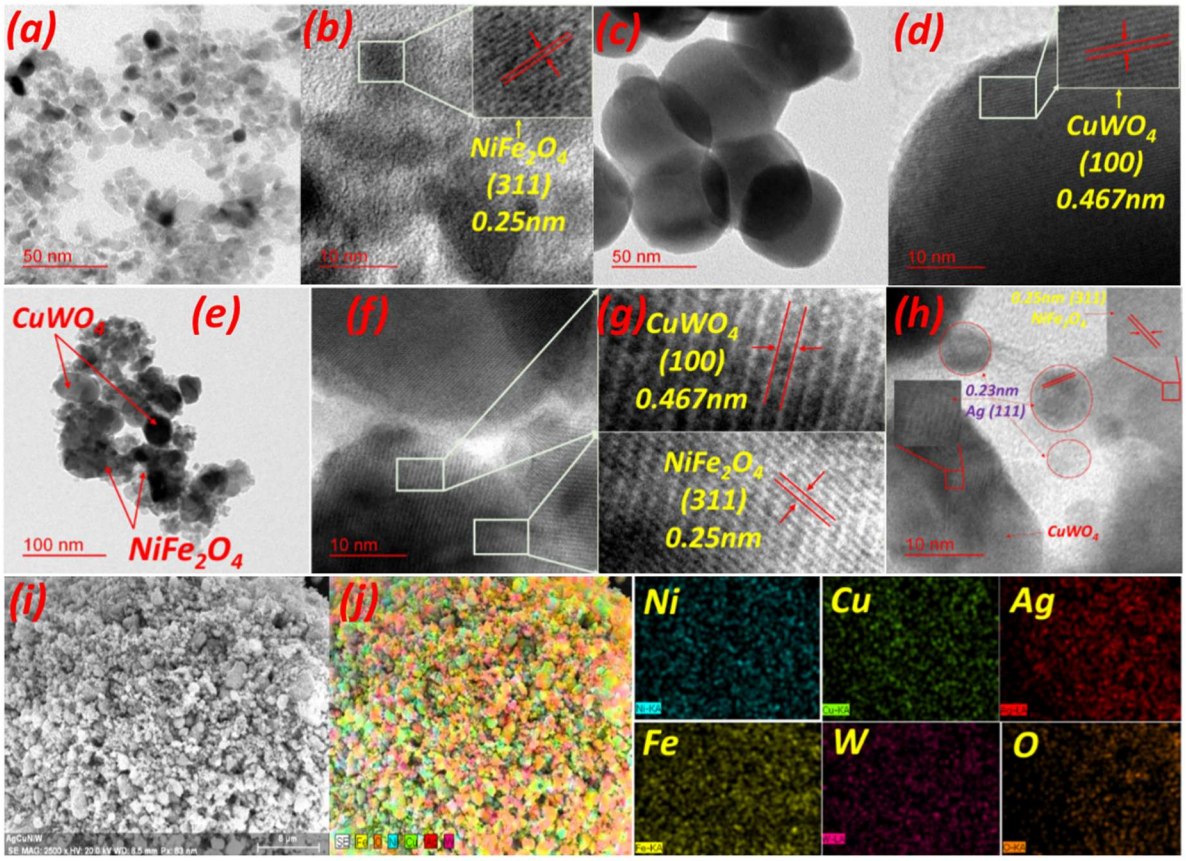


**Figure 4.3** TEM and HR-TEM images display the typical morphologies of **(a, b)** $NiFe_2O_4$ and **(c, d)** $CuWO_4$ nanoparticles. **(e, f )** TEM and HR-TEM images of the $CuWO_4$/$NiFe_2O_4$ nanocomposites and **(g)** show the IFFT images of the $CuWO_4$/$NiFe_2O_4$ composite. HR-TEM image of the U1 sample displays adjacent $CuWO_4$ and $NiFe_2O_4$ crystal planes. The **(h)** TEM images of the 5AgU1 composite nanoparticles. **(i, j)** SEM images and their corresponding elemental mapping.

Figure 4.4a displays the solid-state UV-visible absorbance plots of $CuWO_4$ and $NiFe_2O_4$ samples. The Tauc plots for determining the optical bandgaps of $CuWO_4$ and $NiFe_2O_4$, constructed using the absorbance data, are given in Fig. 4.4b and 4.4c, respectively. Equation (4.1) states the Tauc relation.

$$(\alpha h\upsilon)^{1/n} = A\,(h\upsilon - E_g) \qquad (4.1)$$

In this equation, α represents the molar absorption coefficient, n depicts the transition exponent, and $E_g$ gives the bandgap energy [155]. The exponent *n* has a value equal to 0.5 for direct transitions and 2 for indirect transitions, while 'A' is a constant. A straight line is fitted to the linear region of the plot between $(\alpha h\upsilon)^{1/n}$ and hυ. The point at which this fit intercepts the x-axis is the optical bandgap energy. The bandgaps of $CuWO_4$ and $NiFe_2O_4$ found from these plots are 2.35 eV (indirect) and 1.97 eV (direct), respectively.

The band edge potentials and semiconductor types of $CuWO_4$ and $NiFe_2O_4$ nanoparticles are determined by MS plots [156,157]. The positive slopes of the $CuWO_4$ and $NiFe_2O_4$ MS plots show that both are n-type semiconductors (Figure 4.4 (d, e)). The CB positions of $CuWO_4$ and $NiFe_2O_4$ nanoparticles are 0.38 V and -0.79 V, respectively. Respective VB positions were calculated by combining the MS results with the band gap of the $CuWO_4$ and $NiFe_2O_4$ using the equation $E_{CB}=E_{VB}-E_g$. Using this formula, the VB positions of $CuWO_4$ and $NiFe_2O_4$ are 2.73 and 1.18 V, respectively.

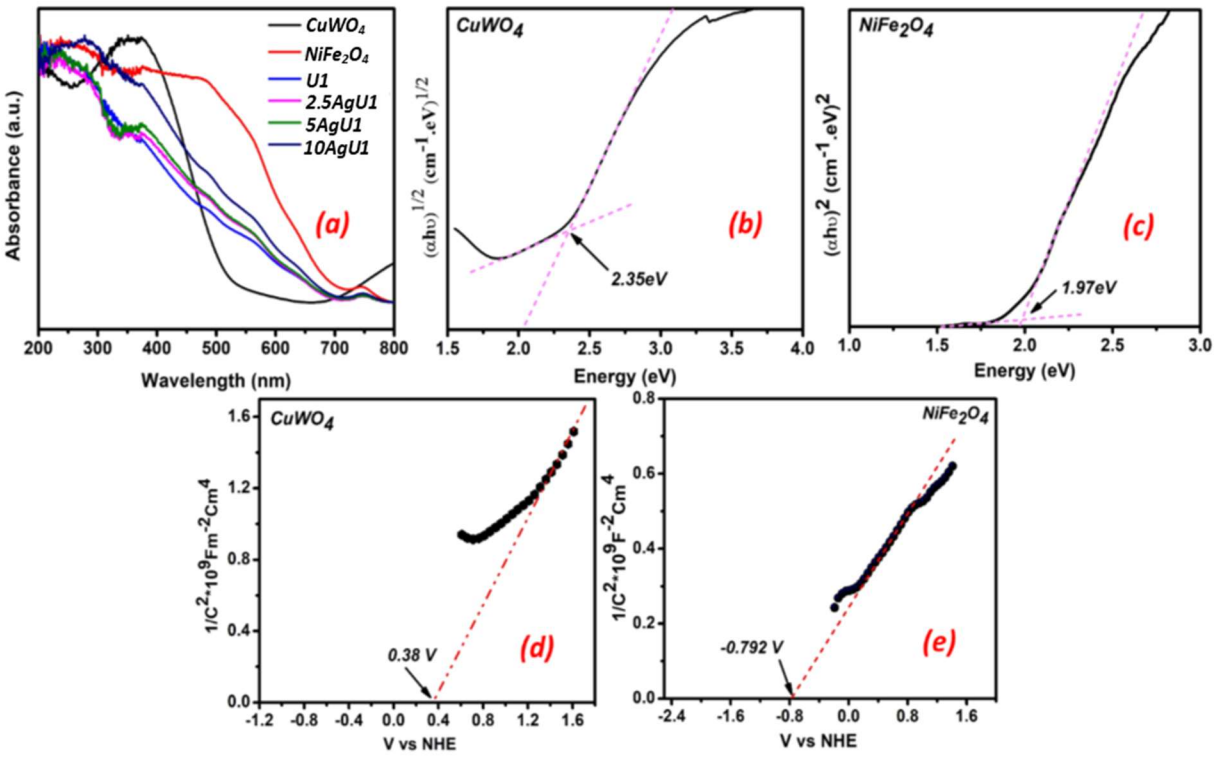

**Figure 4.4 (a)** Solid-state UV-visible absorbance plots of all prepared photocatalysts. Tauc plots of **(b)** $CuWO_4$ and **(c)** $NiFe_2O_4$. Mott Schottky plots of **(d)** $CuWO_4$ and **(e)** $NiFe_2O_4$.

XPS analysis of the 5AgU1 composite nanoparticles revealed the chemical states and surface compositions. The 5AgU1 composite photocatalyst exhibits Cu 2p, W 4f, Ni 2p, Fe 2p, O 1s, and Ag 3d peaks, confirming Ag/$CuWO_4$/$NiFe_2O_4$ nanocomposite formation. The C1s peak in the survey spectrum mainly came from hydrocarbon contaminants, normally present in an XPS spectrum [158]. The HR-XPS spectrum of Cu 2p shows the three characteristic peaks for Cu $2p_{3/2}$ and Cu $2p_{1/2}$ at 932.7, 934.2, and 953.1 eV (Figure 4.5a), typical of $Cu^{2+}$ oxidation states present in the lattice sites of $CuWO_4$. Furthermore, two satellite peaks were observed at 942.6 and 962.5 eV due to Cu(II) in the cupric compound [159]. The W $4f_{7/2}$, W $4f_{5/2,}$ and W $5p_{3/2}$ peaks at 35.29, 37.42, and 41.02 eV are due to the $W^{+6}$ oxidation state (Figure 4.5b) of tungsten. The deconvoluted spectrum of Ni 2p (Figure 4.5c) at the binding energies 854.87, 856.15, and 872.9 eV corresponds to the Ni $2p_{3/2}$ and Ni $2p_{1/2,}$ respectively, which denote the $Ni^{2+}$ oxidation states [160]. The Fe 2p fitted spectrum (Figure 4.5d) shows 710.5, 712.5, and 724.86 eV spin-orbit peaks of Fe $2p_{3/2}$ and Fe $2p_{1/2}$ due to the $Fe^{3+}$ oxidation state in the $NiFe_2O_4$ photocatalyst [161]. The high-resolution O 1s plot could be deconvoluted into four characteristic contributions at 532.6, 531.3, 530.2, and 529.6 eV. These were ascribed to the physically and chemically adsorbed oxygen and surface hydroxyl groups. The peak at 529.6 eV (Figure 4.5e) is due to lattice oxygen [162]. The binding energy of Ag 3d at 368.2 and 374.2 eV suggests the formation of pure silver (metallic Ag) over the composite sample (Figure 4.5f).

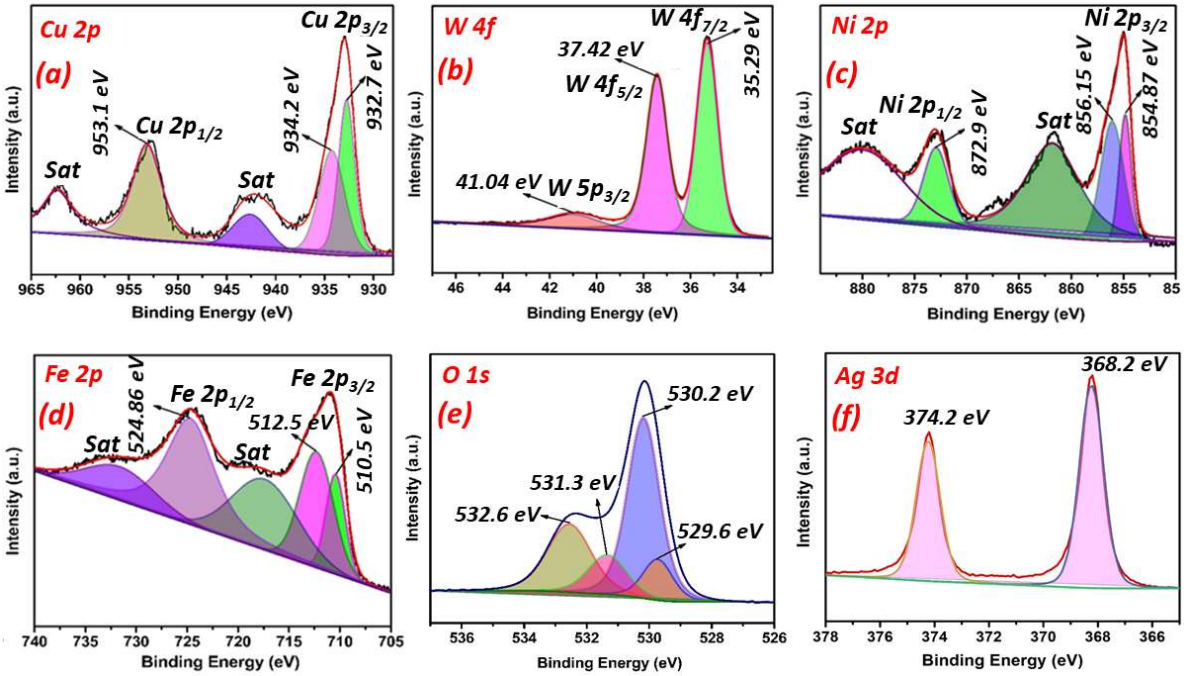


**Figure 4.5** XPS spectra of 5AgU1 sample **(a)** Cu 2p**, (b)** W 4f**, (c)** Ni 2p**, (d)** Fe 2p**, (e)** O 1s**, (f)** Ag 3d.

PL spectra compare the relative electron-hole recombination efficiencies. The spectrum with the lowest peak emission intensity has the slowest electron-hole recombination. The 5AgU1 photocatalyst has the lowest PL spectrum intensity (Fig. 4.6a). It indicates five wt. % loading of silver nanoparticles on U1 composite photocatalyst enhances the charge carrier separation and reduces recombination. Figure 4.6b displays the Nyquist plots of ($CuWO_4$/$NiFe_2O_4$) U1, and 5AgU1 samples. The 5AgU1 photocatalyst plot exhibits the smallest arc radius among all samples. It implies that the 5AgU1 composite has lower resistance and better interfacial charge transfer than other samples in this study [163].

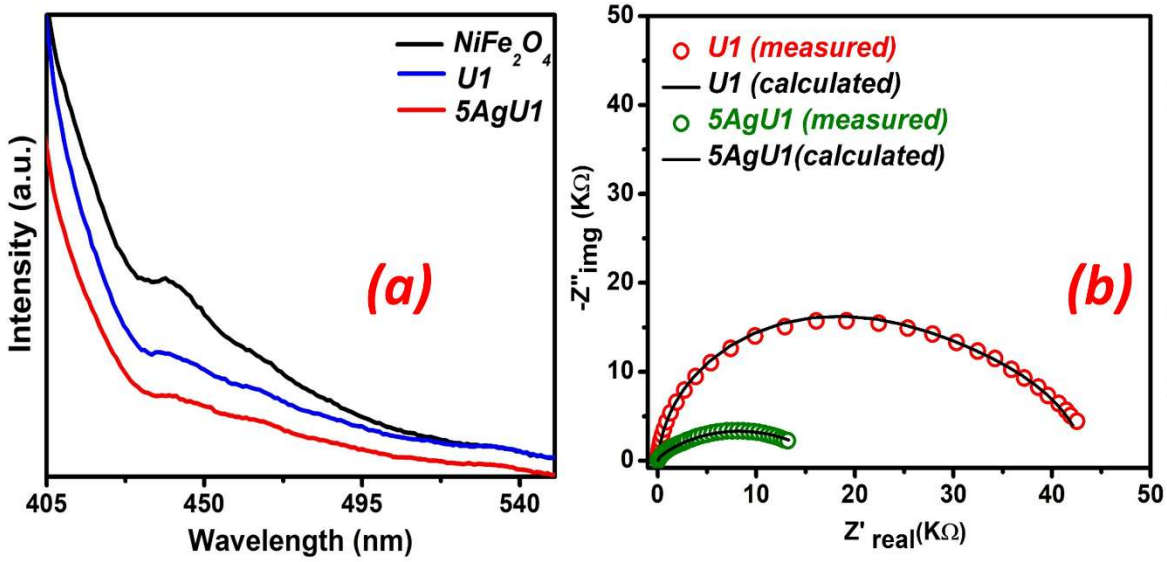


**Figure 4.6 (a)** PL spectra of $NiFe_2O_4$, U1 and 5AgU1 photocatalysts (b) Nyquist plot of the U1 and 5AgU1 sample.

Figure 4.7 shows the magnetic moment versus applied magnetic field plots of the U1 and 5AgU1 samples at room temperature. The hysteresis loops have almost no coercivity and remanence, demonstrating that these samples are superparamagnetic. Saturation magnetizations ($M_S$) of U1 and 5AgU1 are 15.49 and 13.30 emu/g, respectively. The reduction in the $M_S$ value of the 5AgU1 sample is because of the incorporation of non-magnetic silver nanoparticles in the U1 composite sample. The inset images in Figure 4.7 show that a magnetic field can quickly recover the samples from the treated aqueous solution.

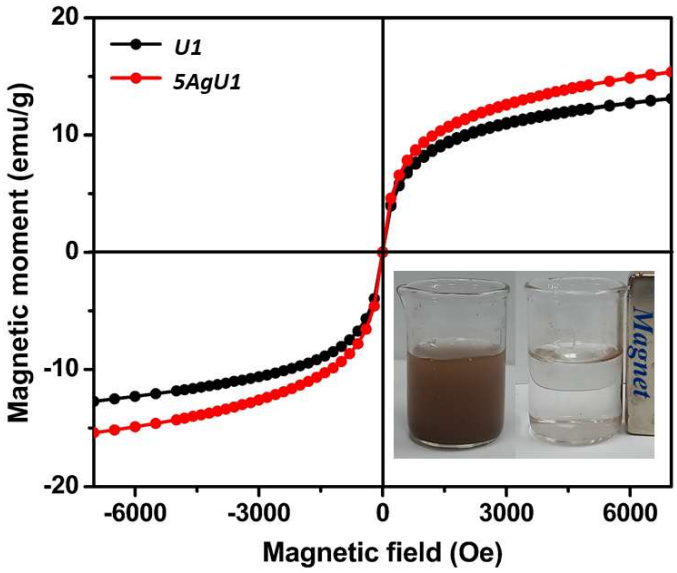


**Figure 4.7** Magnetic measurements of U1 and 5AgU1 photocatalysts.

### 4.3.1 Molecular Dynamics Results

The oxygen adsorption aspects of the mechanism of efficient $H_2O_2$ production on the designed photocatalyst were investigated by MD simulations. Figures 4.8a and 4.8b show the $NiFe_2O_4$ and $CuWO_4$ models after ten nanoseconds (ns) MD simulations. The picture indicates that oxygen molecules are mainly near the $NiFe_2O_4$ surface. In contrast, the oxygen molecules are located away from the $CuWO_4$ surface. Figure 4.9 gives the long-time average density profiles of oxygen molecules with distance (along the z-axis) from the $NiFe_2O_4$ and $CuWO_4$ surfaces. There is only one oxygen molecule peak on either side of the $NiFe_2O_4$ slab. These peaks neighbor the $NiFe_2O_4$ slab surface and show the adsorption of the oxygen molecules on the $NiFe_2O_4$ surface. Comparatively, the intensity of the oxygen molecules peak adjacent to the $CuWO_4$ surface is significantly less. The results show that oxygen molecules have a stronger interaction with the $NiFe_2O_4$ surface than the $CuWO_4$ slab.

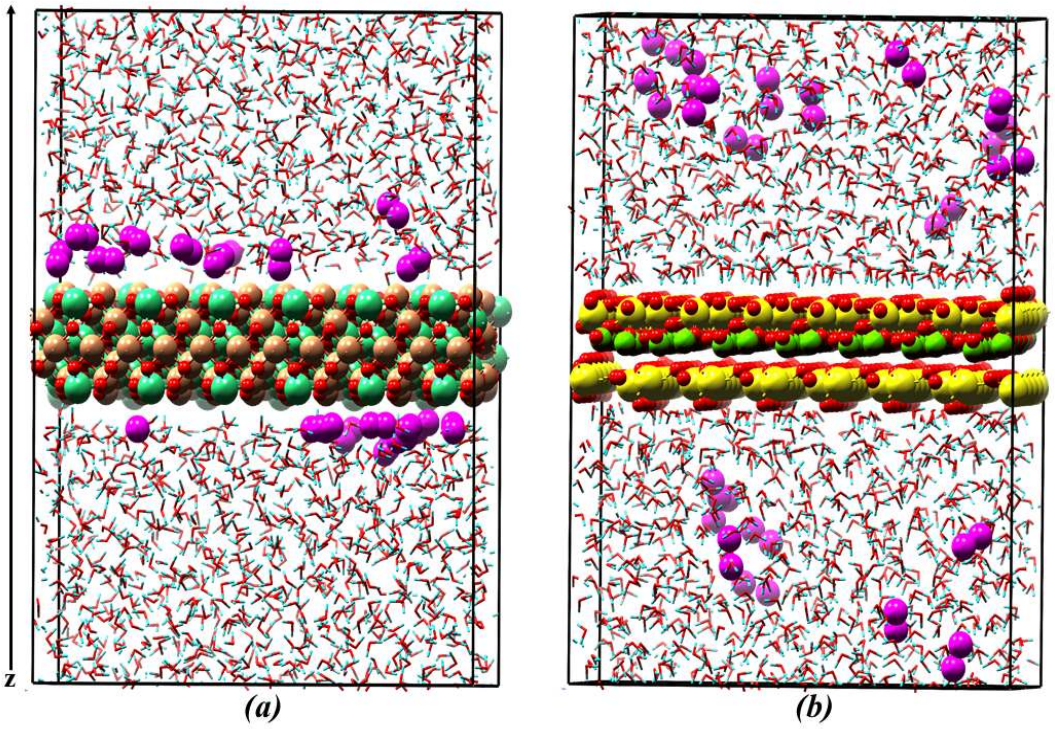


**Figure 4.8 (a, b)** The snapshot of the final configuration after 10ns MD simulation (left side-$NiFe_2O_4$ (311) & right side $CuWO_4$ (100).

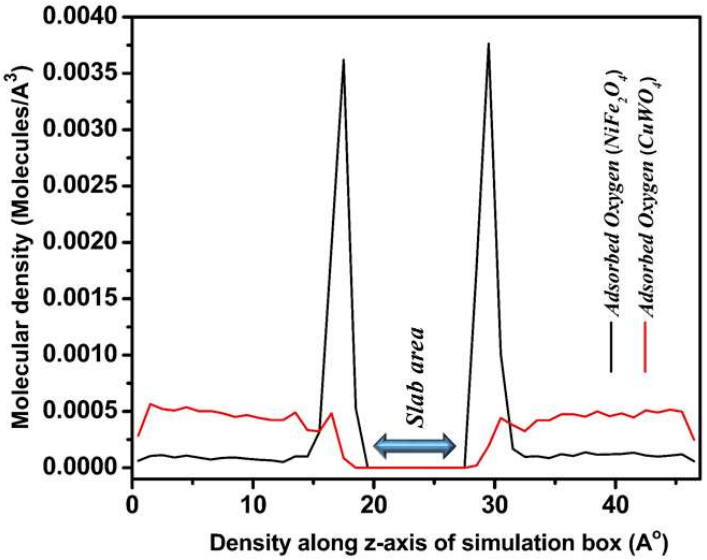


**Figure 4.9** Density profiles of oxygen molecules on $CuWO_4$ (100) and $NiFe_2O_4$ (311) surfaces along the z-directions of the simulation box.

Here, RDF analysis has been employed to understand the interaction of oxygen and water molecules with the atom types on respective adsorbent ($NiFe_2O_4$ (311) and $CuWO_4$ (100)) surfaces. The RDF data were calculated from the long-time average data obtained from the production run part of the MD simulation. Figure 4.10a shows the RDF of oxygen with different atom types in $CuWO_4$ and $NiFe_2O_4$ surfaces. The first intense peak is at ~2.2 Å distance due to the Ni($NiFe_2O_4$)-O($O_2$) interaction. The second high-intensity peak occurs at ~3.08Å distance because of the Fe($NiFe_2O_4$)-O($O_2$) interaction. These plots demonstrate that oxygen molecules interact primarily with the Ni atom types on the $NiFe_2O_4$ surface. Figure 4.10a also displays the two $O_2$-$CuWO_4$ RDF plots. These show that oxygen molecules interact weakly with Cu atoms in the $CuWO_4$ slab. The peak for this interaction occurs at a distance greater than 4Å. Figure 4.10b gives the RDF plots between the atom types in water molecules and those in $NiFe_2O_4$ and $CuWO_4$ surfaces. The first (green plot) peak at 1.49 Å shows an interaction between the oxygen of $CuWO_4$ and hydrogen of water (O_M($CuWO_4$-H_W(water)). This peak occurs at a typical hydrogen bond distance. The second peak at ~2.08 Å (pink) is between the W atom of $CuWO_4$ and the oxygen of water molecules. The other peak between Cu of $CuWO_4$ and oxygen of water is a secondary peak and occurs at a much larger distance (~4.3Å). The rest of the low-intensity RDF peaks corresponding to Ni-O_W, Fe-O_W, and O_3-H_W interaction represent poor water and $NiFe_2O_4$ surface interaction. One can conclude that the $NiFe_2O_4$ surface interacts strongly with oxygen molecules in an aqueous medium, while $CuWO_4$ has a greater water adsorption affinity.

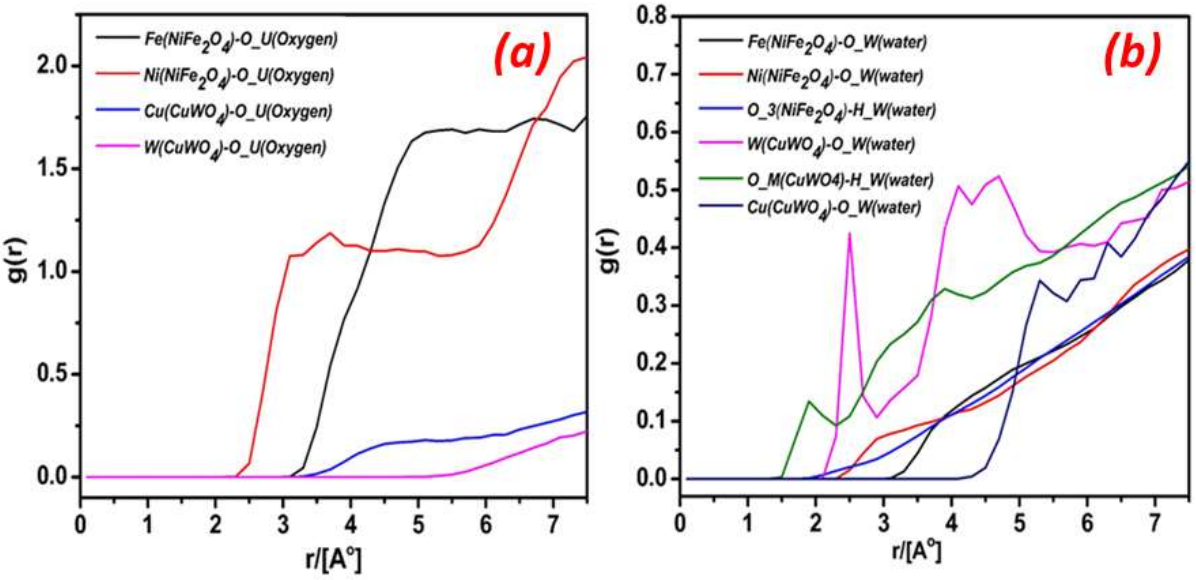


**Figure 4.10** RDF plots of interactions between atom types in $O_2$ and $H_2O$ with those in $NiFe_2O_4$ (311) and CuWO4 (100) slabs. In the graph, atom types are labeled by specific symbols. Fe ($NiFe_2O_4$), Ni ($NiFe_2O_4$), and O_3 ($NiFe_2O_4$) represent nickel, iron, and oxygen atoms of $NiFe_2O_4$. Similarly, W ($CuWO_4$), Cu ($CuWO_4$), and O_M ($CuWO_4$) depict tungsten, copper, and oxygen atoms types of $CuWO_4$. O_U represents the oxygen atoms in oxygen molecules. H_W and O_W are hydrogen and oxygen atom types in water molecules.

### 4.3.2 Photocatalytic $H_2O_2$ production performance

A series of experiments were conducted to investigate $H_2O_2$ formation under different conditions. Firstly, the aqueous suspensions of different materials prepared in this study were kept in the dark for one hour. No $H_2O_2$ production was detected. Next, the aqueous suspensions of all samples were tested for $H_2O_2$ production after exposing them to visible light irradiation for one hour. $H_2O_2$ detected after this exposure was negligible. In subsequent experiments, the aqueous suspensions of different samples were subjected to visible light irradiation along with continuous passing of oxygen for one hour. No $H_2O_2$ production was detected with the pure $CuWO_4$ and $NiFe_2O_4$. But, significant $H_2O_2$ formation was detected in aqueous suspensions of samples U1, 2.5AgU1, 5AgU1, and

10AgU1 (Table 4.1**)**. Among these, sample 5AgU1 photocatalyst exhibited the best $H_2O_2$ production activity at pH 3. $H_2O_2$ formation decreased with a further increase in Ag loading on the U1 composite. Thus, increased Ag percentage on the U1 photocatalyst (beyond the 5wt% level) hindered visible light absorption by the semiconductor components. The dependence of $H_2O_2$ production on the solution pH was investigated by carrying out experiments at three different pH values (1, 3, and 5). Figure 4.11a shows that sample 5AgU1 exhibited the highest photocatalytic $H_2O_2$ production activity at pH 3. The pH 1 solution provides excess protons ($H^+$) to the reaction medium, and the $H_2O_2$ formed can undergo oxidization to water ($H_2O_2 + 2H^+ + 2e^- = 2H_2O$). Alternatively, the pH 5 condition provides fewer protons, causing lower $H_2O_2$ formation. Hence, pH 3 was the optimum value of pH for $H_2O_2$ production. Photocatalytic $H_2O_2$ formation was also evaluated after adding ethanol (EtOH) in the same solution (5-volume% EtOH/water +$O_2$). The $H_2O_2$ production activity increased by approximately 48.2%. Similarly, adding 5-vol% IPA in the photocatalytic solution (5volume% IPA/water+$O_2$) further enhanced $H_2O_2$ productivity by 51.6% compared to pure water with continuous $O_2$ bubbling through the reaction medium. IPA/EtOH acts as an electron donor to quench the photo-excited holes in the VB of the photocatalyst. These results suggest that the $H_2O_2$ is mainly produced by $O_2$ reduction rather than the oxidation of $H_2O$ by the photogenerated holes. Photocatalytic $H_2O_2$ production can occur by one-electron or the two-electron oxygen reduction mechanism. The former, one-electron oxygen reduction, results in superoxide radical formation. Superoxide scavenger tests by adding PBQ to the reaction mixture did not affect the $H_2O_2$ production activity. Thus, superoxide radicals are not reactive species for the considered photocatalytic reaction (Figure 4.11b). Table 4.2 compares the $H_2O_2$ generation rates on photocatalyst systems published earlier with those of the 5AgU1 system. A perusal of Table 4.2 shows that 5AgU1 has a high photocatalytic $H_2O_2$ generation activity.

**Table 4.1** Photocatalytic $H_2O_2$ formation on the samples prepared in this study.

| **Photocatalyst** | **$H_2O_2$ formed** **µmol. $g^{-1}.h^{-1}$** |
|---|---|
| $CuWO_4$ | No activity |
| $NiFe_2O_4$ | No activity |
| U1 | 360 µmol.g−1.$h^{-1}$ |
| 2.5AgU1 | 780 µmol.$g^{-1}.h^{-1}$ |
| 5AgU1 | 930 µmol.$g^{-1}.h^{-1}$ |
| 10AgU1 | 656 µmol.$g^{-1}.h^{-1}$ |

**Table 4.2**: Comparison of photocatalytic $H_2O_2$ generations of prepared photocatalysts in this study with another previously reported photocatalytic system in recent years.

| **Photocatalyst** | **Reaction Condition** | **Light Source** | **$H_2O_2$ production (µmol$g^{-1}h^{-1}$)** | **Ref.** |
|---|---|---|---|---|
| Benzene/$K^+$/CN | Water with molecular oxygen ($O_2$) | 300W Xe lamp (λ > 420 nm) | 287.5 | [53] |
| 3F-BN | 5% IPA / distilled water mixture | Visible light (λ > 420 nm) | 729 | [164] |
| SPCN | 10% IPA / distilled water mixture | Visible light (λ > 420 nm) | 323.6 | [165] |
| $WO_3$/CN-SUP | 5% EtOH / distilled water mixture/$O_2$ purging | AM 1.5G | 322 | [132] |
| 5% $ZnIn_2S_4$/FTCN50 | 10% EtOH / distilled water mixture | Visible light (λ > 420 nm) | 135.98 | [166] |

| | | | | |
|---|---|---|---|---|
| SN-GQD-$TiO_2$ | 5% IPA / distilled water mixture | Visible light (λ > 420 nm) | 902 | [167] |
| $K_2HPO$/GCN | 10% EtOH / distilled water mixture | Visible light (λ > 420 nm) | 505 | [168] |
| FeOOH/UPCN | Only water | Visible light (λ > 420 nm) | 29.89 | [60] |
| CdS/$Fe_3O_4$/N-doped C | Only water | 300W Xe lamp (λ > 420 nm) | 47.28 | [134] |
| Ag@U-g-$C_3N_4$-NS | Only water | 300W Xe lamp (λ > 420 nm) | 67.50 | [169] |
| $CoWO_4$@$Bi_2WO_6$ | Water with molecular oxygen ($O_2$) | 300W Xe lamp (λ > 420 nm) | 40 | [130] |
| $Fe_2(MoO_4)_3$/Ag/$Ag_3PO_4$ | Only water<br>Methanol/water mixture | UV-visible light | 273.6<br>400.8 | [141] |
| HDMP grafted g-$C_3N_4$ | 10% IPA / distilled water mixture with $O_2$ bubbling | 300W Xe lamp (λ > 420 nm) | 174 | [170] |
| $TiO_2$ /$In_2S_3$ | $O_2$ saturated water/ 10% EtOH | 300W Xe lamp (28 mW/cm2) | 752 | [171] |
| E-$MoS_2$/$FeS_2$ | Pure water | 300W Xe lamp | 75 | [172] |
| $Fe_2O_3$/$MoS_2$@Ag | Pure water | Visible | 15 | [139] |
| NCQDs/MIL-101(Fe) | Pure water | 500W Xe lamp (λ > 420 nm) | 80 | [173] |
| $Ag_3PO_4$@$NiFe_2O_4$ | 75 vol% MeOH/ water mixture | 300W Xe lamp (λ > 420 nm) | 130 | [174] |

| | | | | |
|---|---|---|---|---|
| 5AgU1 | Water with molecular oxygen ($O_2$) | Cool white LED (1070 $W/m^2$) | 930 | This work |
| | 5% EtOH / distilled water mixture | | 1380 | |
| | 5% IPA / distilled water mixture | | 1410 | |

### 4.3.3 In-situ photo-Fenton degradation of tetracycline

The first experiments on tetracycline degradation by photocatalysis were without oxygen purging (4.11c). These experiments were carried out on all samples prepared in this study. Figure 4.11c shows comparison plots of tetracycline degradation (under visible light) with time on different ($CuWO_4$, $NiFe_2O_4$, U1, 2.5AgU1, 5AgU1, and 10AgU1) samples. These experiments were conducted without passing oxygen through the reaction medium. Photocatalytic tetracycline degradation follows second-order rate kinetics (Figure 4.11d). The 5AgUI nanoparticles demonstrated better photocatalytic activity for tetracycline degradation (without oxygen passing) than other composites. Scavenger experiments on the 5AgUI sample showed that holes and superoxide radicals are active species (Figure 4.11e). Figure 4.11f compares photocatalytic tetracycline degradation activity under different reaction conditions. No tetracycline degradation occurred in the absence of a photocatalyst. The photocatalyst for the rest of the experiments in this figure was 5AgUI. Continuous oxygen passing through the reaction medium significantly improved the tetracycline degradation activity (over the case of no oxygen purging). The degradation activity increased upon adding ethanol and IPA to the reaction medium with continuous oxygen bubbling. Figure 4.11g shows the effect of different scavengers on tetracycline degradation (over 5AgUI) under oxygen-passing conditions. The addition of PBQ did not change the photocatalytic activity. Hence, superoxide radicals had no role in tetracycline degradation for photocatalysis under oxygen-passing conditions. Additionally, nitroblue

tetrazolium chloride (NBT) was used to detect superoxide radicals under continuous $O_2$ bubbling and in the absence of oxygen purging. In the absence of $O_2$ bubbling, a robust formation of superoxide radicals occurs (Figure 4.11h). But under a continuous flow of oxygen, the $^{\cdot}O_2^-$ (superoxide) formation diminishes (Figure 4.11i) significantly. Thus, superoxide radicals are not active species responsible for $H_2O_2$ production under oxygen-purging conditions. Given the negligible role of superoxide radicals, photocatalytic $H_2O_2$ production must be occurring through the 2-electron $O_2$ reduction mechanism under a continuous flow of oxygen. Additionally, Table 4.2 compares the present work with earlier publications mentioning the Fenton activity of different photocatalysts reporting $H_2O_2$ production. The Fenton degradation activity of 5AgUI is higher than the majority of earlier reported photocatalysts. Thus, the 5AgU1 sample may be a promising photocatalyst for the self-Fenton-like catalytic reactions for the degradation of organic pollutants.

Reusing photocatalysts after the reaction is essential for practical and industrial applications. Figure 4.11j shows that the photocatalyst performance was nearly unchanged after five cycles. Furthermore, the mass (catalyst loss) of the photocatalyst was measured after each cycle, and the catalyst loss was almost negligible. Compared to the first cycle, tetracycline degradation activity decreased by approximately 4.5% in the fifth cycle, indicating that the photocatalyst is completely recovered by magnetic decantation. In addition, the powder diffraction XRD was conducted on the reused 5AgUI sample. All phases in the fresh sample were also present in the reused 5AgUI sample. No extra peaks were observed, indicating the stability of the 5AgUI sample after its reuse (Figure 4.11k).

**Table 4.3** A Comparison table of the self-Fenton degradation system on 5AgU1 photocatalyst prepared in this study with another previously reported photocatalytic system.

| Photocatalyst | Pollutant amount | Light source | Degradation% % and time | Ref |
|---|---|---|---|---|

| | | | | |
|---|---|---|---|---|
| FeOCl/CDots | 5ppm (p-chlorophenol) | 150W Xe lamp ($\lambda > 420$ nm) | 90.1%(180min) | [54] |
| HDMP grafted $gC_3N_4$ | 20ppm (Oxytetracycline hydrochloride) | 300W Xe lamp ($\lambda > 420$ nm) | 79.8 % (120min) | [170] |
| g-$C_3N_4$ /PDI/Fe | 10ppm (p-nitrophenol) | 300W Xe lamp ($\lambda > 420$ nm) | 80% (60min) | [175] |
| FeOOH/UPCN | 20ppm (Oxytetracycline) | 300W Xe lamp ($\lambda > 420$ nm) | 86.23%(120min) | [60] |
| $Fe_2O_3/MoS_2$@Ag | 10ppm (2,4Dichloropheno) | Visible | 99% (150min) | [139] |
| (Fe)NCQDs/MIL-101 | 10ppm (Tetracycline) | 500W Xe lamp ($\lambda > 420$ nm) | 100% (180min) | [173] |
| Ag/s-($Co_3O_4/NiFe_2O_4$) | 10ppm (Tetracycline) | Cool white LED (1070 W/$m^2$) | ~99% (400min) | [49] |
| 5AgU1 | 10ppm (Tetracycline) | Cool white LED (1070 W/$m^2$) | 93% (60min) | This work |

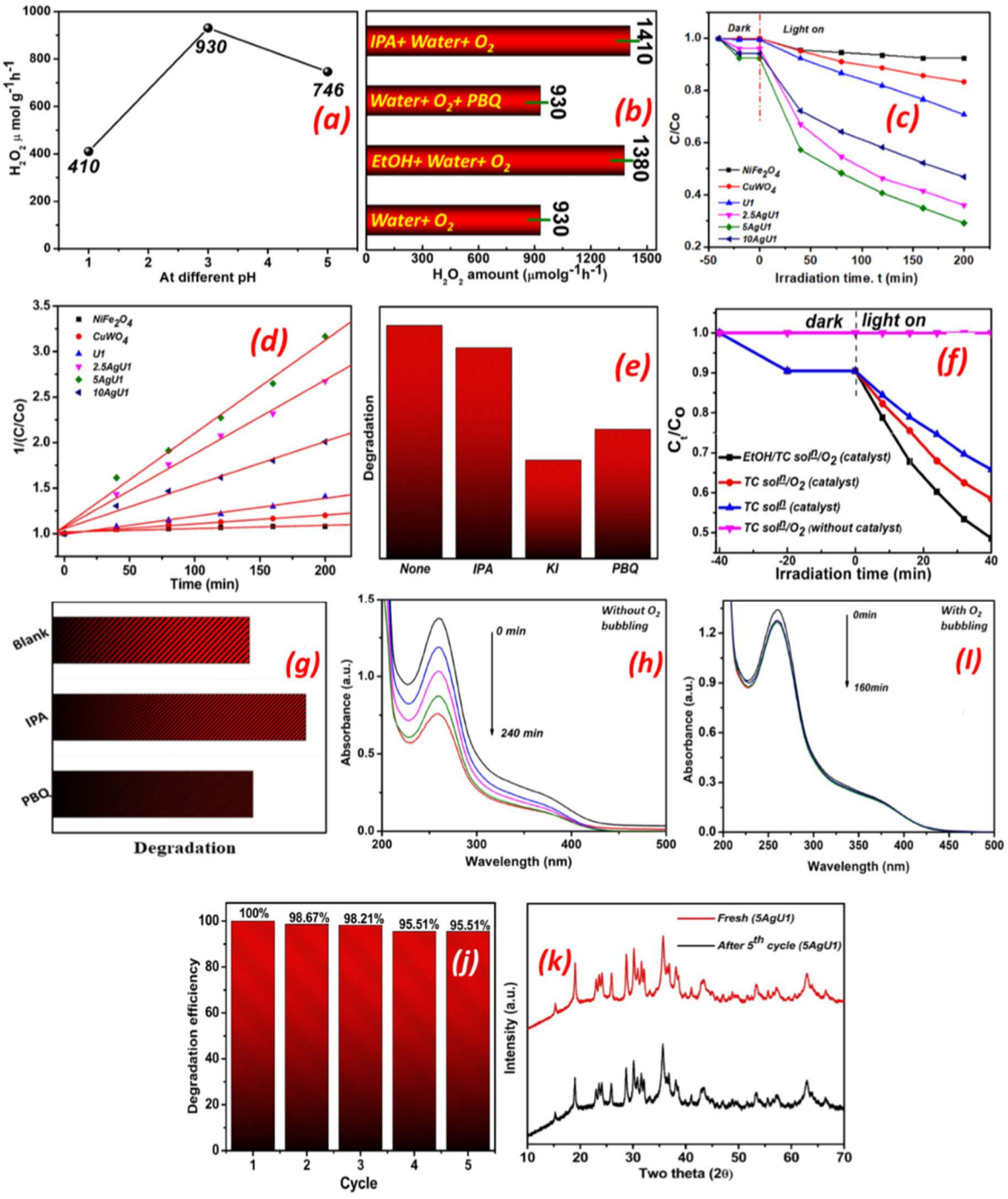


**Figure 4.11** Photocatalytic **(a)** $H_2O_2$ formation at three different pH levels and **(b)** $H_2O_2$ formation under different control conditions. **(c)** Comparison plot of tetracycline degradation with time on all prepared photocatalysts **(d)** Second-order reaction kinetics plot for tetracycline degradation on different photocatalysts. **(e)** Trapping experiment for degradation of tetracycline on 5AgU1 photocatalyst **(f)** Comparison plot of tetracycline

degradation with time under different control conditions on 5AgU1 photocatalyst. **(g)** Trapping experiment for degradation of tetracycline on 5AgU1 photocatalyst under oxygen purging. UV-vis absorbance spectra of 2.5x $10^{-5}$ mol/L NBT aqueous solution containing 5AgU1 photocatalyst **(h)** without $O_2$ bubbling **(i)** with $O_2$ bubbling. **(j)** The bar plot of tetracycline degradation for the continuous reuse of the 5AgU1 sample five times**. (k)** XRD pattern of the recycled photocatalyst.

### 4.4 Investigation of the photocatalytic mechanism

This section proposes the photocatalytic reaction mechanism for $H_2O_2$ production and tetracycline degradation (Figure 4.12). Combining experimental and molecular dynamics simulation results helped us arrive at this mechanism. The PL and EIS measurements revealed that the 5AgU1 sample possesses poor photo-excited species recombination ability and faster interfacial charge transfer efficiency. Furthermore, the 5AgU1 photocatalyst displayed the best $H_2O_2$ production and tetracycline degradation performance compared to other prepared photocatalysts.

The detection of superoxide radicals on UI and other composites during scavenger experiments (without passing oxygen) points to one-electron oxygen reduction on the $NiFe_2O_4$ part of the composite. Classical MD simulations also show that oxygen prefers to adsorb on the $NiFe_2O_4$ surface. Moreover, $CuWO_4$ and $NiFe_2O_4$ are both n-type semiconductors. Electrons were supplied to the VB side by tetracycline oxidation on the photoexcited holes. The pieces of evidence reinforce the idea of Z-scheme photocatalysis. The schematic in Figure 4.12 describes the proposed mechanism. The illumination of photocatalyst (5AgU1) with visible light photo-excites electrons from the valence bands of $CuWO_4$ and $NiFe_2O_4$ to their conduction bands. Photo-excited electrons of the $CuWO_4$ recombine with the holes in the VB of $NiFe_2O_4$. Ultimately, the photo-excited holes are

concentrated in the $CuWO_4$ VB, and the electrons migrate to the $NiFe_2O_4$ CB by a Z-scheme pathway. However, Ag nanoparticles, deposited over $CuWO_4$ and $NiFe_2O_4$, act as electron-capturing centers and provide sites for $O_2$ reduction. Another possibility is that Ag NPs in contact with $NiFe_2O_4$ and $CuWO_4$ components can transfer charges between the two components. The photo-excited electron ($e^-$) can move from the CB of $CuWO_4$ to Ag NPs. These electrons can then migrate from Ag to the VB of $NiFe_2O_4$, fulfilling a Z-scheme mechanism.

Note that $H_2O_2$ production happens only on continuous oxygen passing through the reaction medium. The 2-electron oxygen reduction necessary for $H_2O_2$ formation is slower than the one-electron pathway for superoxide formation. Constant oxygen passing reduces the kinetic barrier to facilitate $H_2O_2$ production. The $H_2O_2$ produced by photocatalysis is reductively cleaved on the $NiFe_2O_4$ surface by a Fenton-like mechanism. The hydroxyl radicals oxidize tetracycline, while the $OH^-$ (hydroxide) anions get oxidized on the $CuWO_4$ VB (reduction potential of $OH^-$/ •OH is 1.99 V). Note that the VB of $CuWO_4$ is approximately 2.42 eV. Tetracycline degradation by photocatalysis was higher in 5-vol% ethanol solution with $O_2$ purging due to increased $H_2O_2$ production. Ethanol was the electron source for oxidation by holes in the $CuWO_4$ VB. More significant number of •OH radicals were formed by a Fenton-like reductive cleavage reaction, causing enhanced tetracycline degradation activity.

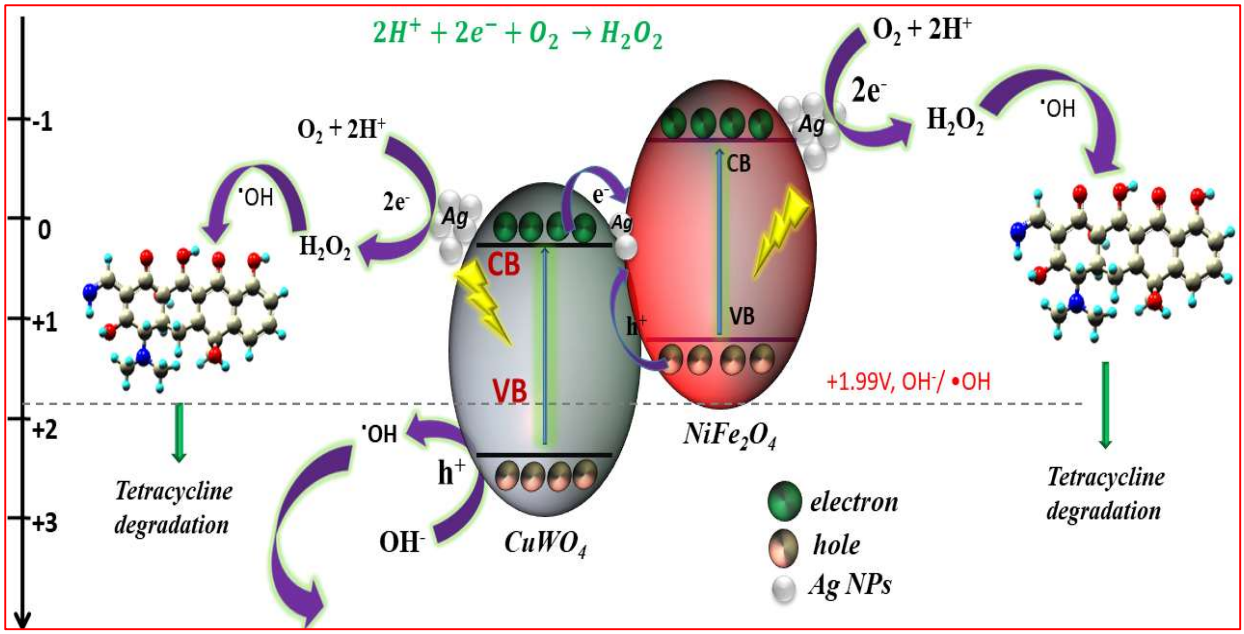


**Figure 4.12.** Proposed mechanism of photocatalytic $H_2O_2$ production and insitu-Fenton degradation of the tetracycline molecule.

## 4.5 Conclusions

A composite photocatalyst Ag/$CuWO_4$/$NiFe_2O_4$ for $H_2O_2$ production from pure water has been designed and evaluated. Following a step-wise precipitation protocol, $CuWO_4$ nanostructures were precipitated on $NiFe_2O_4$ nanoparticles. Next, Ag nanoparticles were loaded on the available surfaces of the composite. The composite follows a Z-scheme photocatalysis pathway. The $NiFe_2O_4$ part is the reduction component of the composite since it has a more negative CB (NHE scale). For efficient reduction of oxygen, its adsorption is desired on the reduction component of the Z-scheme photocatalyst. Large-scale classical MD showed oxygen adsorbs preferentially to the $NiFe_2O_4$ surface compared to the $CuWO_4$ side.

Continuous oxygen passing through the reaction mixture gives rise to substantial $H_2O_2$ formation. The superoxide scavenger test did not have any effect on the $H_2O_2$ produced, suggesting a two-electron oxygen reduction pathway. Using isopropyl alcohol or

ethanol as the electron donor (under oxygen-passing) further increased $H_2O_2$ formation. These results showed that oxygen reduction was the rate-limiting step for $H_2O_2$ production. Photocatalysis of tetracycline degradation was attempted with and without oxygen passing. The degradation was substantially enhanced under oxygen-passing and ethanol-diluted reaction medium conditions, implying an in-situ Fenton-like reaction mechanism.